Acta Biomaterialia 155 (2023) 654–666

Contents lists available at ScienceDirect

Acta Biomaterialia

journal homepage: www.elsevier.com/locate/actbio

Full length article

Antibacterial effect of 3D printed mesoporous bioactive glass scaffolds doped with metallic silver nanoparticles

Sandra Sánchez-Salcedo[a,b], Ana García[a,b,*], Adela González-Jiménez[a], María Vallet-Regí[a,b,*]

[a] Departamento de Química en Ciencias Farmacéuticas, Unidad de Química Inorgánica (Bioinorgánica y Biomateriales), Universidad Complutense de Madrid, Instituto de Investigación Sanitaria Hospital 12 de Octubre i+12. Plaza Ramón y Cajal s/n, 28040 Madrid, Spain
[b] CIBER de Bioingeniería, Biomateriales y Nanomedicina, CIBER-BBN, Madrid, Spain

ARTICLE INFO

Article history:
Received 29 June 2022
Revised 20 October 2022
Accepted 21 October 2022
Available online 1 November 2022

Keywords:
Mesoporous bioactive glasses
Metallic silver nanoparticles
3D scaffolds
Hierarchical porosity
Antibacterial properties

ABSTRACT

The development of new biomaterials for bone tissue regeneration with high bioactivity abilities and antibacterial properties is being intensively investigated. We have synthesized nanocomposites formed by mesoporous bioactive glasses (MBGs) in the ternary SiO_2, CaO and P_2O_5 system doped with metallic silver nanoparticles (AgNPs) that were homogenously embedded in the MBG matrices. Ag/MBG nanocomposites have been directly synthesized and silver species were spontaneously reduced to metallic AgNPs by high temperatures (700 °C) obtained of last MBG synthesis step. Three-dimensional silver-containing mesoporous bioactive glass scaffolds were fabricated showing uniformly interconnected ultrapores, macropores and mesopores. The manufacture method consisted of a combination of a single-step sol–gel route in the mesostructure directing agent (P123) presence and a biomacromolecular polymer such as (hydroxypropyl)methyl cellulose (HPMC) as the macrostructure template, followed by rapid prototyping (RP) technique. Biological properties of Ag/MBG nanocomposites were evaluated by MC3T3-E1 preosteoblastic cells culture tests and bacterial (*E. coli* and *S. aureus*) assays. The results showed that the MC3T3-E1 cells morphology was not affected while preosteoblastic proliferation decreased when the presence of silver increased. Antimicrobial assays indicated that bacterial growth inhibition and biofilm destruction were directly proportional to the increased presence of AgNPs in the MBG matrices. Furthermore, *in vitro* co-culture of MC3T3-E1 cells and *S. aureus* bacteria confirmed that AgNPs presence was necessary for antibacterial activity, and AgNPs slightly affected cell proliferation parameters. Therefore, 3D printed scaffolds with hierarchical pore structure and high antimicrobial capacity have potential applications in bone tissue regeneration.

Statement of significance

This study combines three key scientific aspects for bone tissue engineering: (i) materials with high bioactivity to repair and regenerate bone tissue that (ii) contain antibacterial agents to reduce the infection risk (iii) in the form of three-dimensional scaffolds with hierarchical porosity. Innovative methodology is described here: sol-gel method, which is employed to obtain mesoporous bioactive glass matrices doped with metallic silver nanoparticles where different polymer templates facilitate the different size scales presence, and rapid prototyping technique that provides ultra-large macroporosity according to computer-aided design. The dual scaffolds obtained are biocompatible and deliver active doses of silver capable of combating bone infections, which represent one of the most serious complications associated to surgical treatments of bone diseases and fractures.

* Corresponding authors at: Departamento de Química en Ciencias Farmacéuticas, Unidad de Química Inorgánica (Bioinorgánica y Biomateriales), Universidad Complutense de Madrid, Instituto de Investigación Sanitaria Hospital, 12 de Octubre i+12. Plaza Ramón y Cajal s/n, 28040 Madrid, Spain.
E-mail addresses: anagfontecha@ucm.es (A. García), vallet@ucm.es (M. Vallet-Regí).

https://doi.org/10.1016/j.actbio.2022.10.045

1. Introduction

Bones, as connective tissues, are composed mainly of living cells, a collagenous matrix and mineral substances composed primarily of calcium and phosphate [1]. Reducing damage caused by trauma and the treatment of possible subsequent infections is one of a main challenge in bone tissue engineering. In addition, the number of implant-associated infections has grown considerably due to increasing number of implanted medical devices [2,3]. The management of implant-associated infections is a serious problem with important clinical and socio-economic implications. [4–7]. Bacterial ability to form a biofilm on inert surfaces and adjacent tissues [8,9], led to reduced susceptibility to host defences and antimicrobial therapies. Current treatments usually involves surgery, systemic administration of antibiotics and even implant subtraction, resulting in additional surgery, elongated hospital stays, high secondary effects and increased mortality [10,11].

Bone tissue engineering requires the use of three-dimensional (3D) scaffolds that act as provisional templates to guarantee complete cell colonization for bone tissue regeneration [12–17]. For adequate cell attachment, proliferation and differentiation, scaffolds need to have a 3D interconnected porous hierarchical architecture and a suitable surface chemistry and topography. Since the 1990s, the rapid prototyping (RP) technique has been widely employed [18–24] for the 3D scaffolds manufacture with different scales of porosity that have been previously computer designed. The RP technique consist of a filament obtained by direct ink writing and extruding, from a small needle connected to a cartridge, printing layer by layer the scaffold with designed shape and dimensions by 3D computer-aided design.

Unfortunately, a scaffold is considered a "foreign body", which in an environment with reduced blood supply and local immunodeficiency is likely to favour bacterial colonization of the implant surface. This colonization is the first step towards infection and bacterial infection processes can adversely affect the new bone tissue formation. In the challenging quest for a solution to decrease the possibility of infections associated in bone regeneration process, the use of silver is promising regarding its broad spectrum against planktonic, sessile as well as multidrug-resistant bacteria [25,26]. Silver presence approach could be a crucial phase in the contest against microbial resistance that provide needed alternatives for bone infection treatment. In this sense, silver (ions, particles or nanoparticles) is well-known to have strong inhibitory and bactericidal effects as well as a broad spectrum of antimicrobial activities [27–29]. Studies reveal that silver nanoparticles (AgNPs) bactericidal effect is size and morphology dependent with smaller AgNPs or octahedral and decahedral particles being more potent antibacterial agents [30,31] due to AgNPs also can directly damage and penetrate the cell wall and plasma membrane. In addition, it is widely accepted that the major antibacterial effect of AgNPs is mediated by its partial oxidation which allows the silver ions release into the medium [30,32]. Antibacterial mechanism of silver ions is not clearly defined and there are proposed three main action modes: (i) cause cell lysis by their interact with the peptidoglycan cell wall or with the plasma membrane [33,34]; (ii) prevent DNA replication by their interact with bacterial cytoplasmic DNA [35,36]; (iii) disrupt protein synthesis by their interact with bacterial proteins [33,35]. The different action radii of antibacterial activity is the key to the low bacterial resistance observed in silver and AgNPs.

Mesoporous bioactive glasses (MBGs) are well known materials since 2004 where Chen *et al.* for first published highly ordered MBGs with superior *in vitro* bone-forming bioactivities [37]. MBG materials, based on the ternary system SiO_2–CaO–P_2O_5, have been widely investigated not only for regenerate lost bone but also for antibacterial treatment [38–44]. This dual capability of MBGs is due to the fact that MBGs can be used as drug delivery systems favoring local release on the implantation site due to their ordered mesoporosity, with high surfaces and pore volume [45,46]. The high amount of free silanol groups present on MBG surfaces opens an interesting route for the anchoring of species with antibacterial properties through a covalent attachment [47,48]. A different strategy is the incorporation of ions with different osteogenic or antibacterial properties into MBG matrices [49–54].

Novel materials development based on metal-doped bioceramic 3D scaffolds to decrease the implant-associated infections in bone tissue regeneration is a relevant and current research issue [55–60]. Herein, we report the one-pot synthesis of Ag/MBG nanocomposites as powders or 3D scaffolds formed by MBG matrices homogenously doped with AgNPs following an original methodology. This research work combines sol–gel and supramolecular chemistry to obtain AgNPs-doped MBG matrices and describes the fabrication, by RP technique, 3D computer-aided design scaffolds with uniformly interconnected ultrapores, macropores and mesopores. High temperature treatment facilitates the meso-macroporosity and spontaneously reduces silver species to metallic AgNPs. Optimization of the molar ratios in the Ag/MBG nanocomposite compositions has been carried out to obtain the best conditions for the dual action of Ag/MBG nanocomposites as an antibacterial (*E. coli* and *S. aureus*) and cytocompatible (MC3T3-E1 pre-osteoblastic cells) device.

2. Materials and methods

Sigma-Aldrich provided all chemicals and were used as received, without further purification.

Table S1 (Supplementary Material) summarises the nomenclature and briefly describes all samples.

2.1. Synthesis of mesoporous bioactive glass powders doped with metallic silver nanoparticles (MBG-xAg)

Highly mesostructured nanocomposites formed by ordered mesoporous bioactive glass matrices, in the ternary system SiO_2–CaO–P_2O_5 (85% SiO_2, 10% CaO and 5% P_2O_5 nominal composition), with metallic silver nanoparticles homogeneously embedded inside the matrix were synthetized. For this purpose, the evaporation induced self-assembly (EISA) method [61] was carried out, and a non-ionic surfactant (Pluronic P123) was used as structure-directing agent, and tetraethyl orthosilicate (TEOS), triethyl phosphate (TEP), calcium nitrate tetrahydrate ($Ca(NO_3)_2{\cdot}4H_2O$) and silver nitrate ($AgNO_3$) as sources of SiO_2, P_2O_5, CaO and AgNPs, respectively.

Briefly, in a typical synthesis, 2 g of P123 were dissolved in 30 mL of absolute ethanol with 0.5 mL of HNO_3 (0.5 N). TEOS (3.96 mL), TEP (0.32 mL) and $Ca(NO_3)_2{\cdot}4H_2O$ (0.49 g) were consecutively added in 3 h intervals under continuous stirring at room temperature. Afterwards and in absence of light 10, 25 or 70 mg of $AgNO_3$ were added to obtain the sols that are going to generate MBG-0.15Ag, MBG-0.3Ag or MBG-*1*Ag materials, respectively. The resulting colorless sols were stirred at room temperature overnight, and then they were transferred into Petri dishes (9 cm in diameter) to undergo EISA method in an oven at 30 °C where the gelation process took place. The resulting transparent membranes were calcined at 700 °C in air for 6 h to remove the surfactant, carbonates and nitrates ions, organics residues and specially where Ag^+ cations coming from $AgNO_3$ salt was reduced to metallic silver nanoparticles. Schematic representation of the synthesis procedure was showed in Scheme 1A.

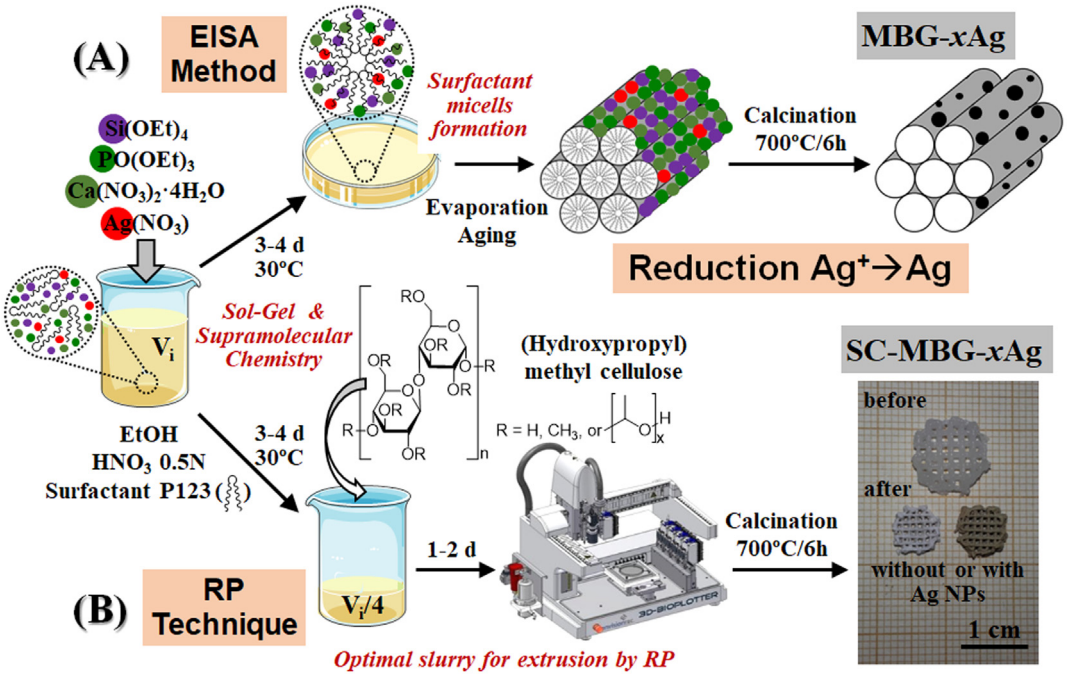

Scheme 1. Schematic representation of different synthesis procedures for **(A)** MBG-*x*Ag powder materials (where •● represent different sizes of AgNPs, ○ mesopores and ■ MBG matrix) and **(B)** SC-MBG-*x*Ag scaffolds.

2.2. Fabrication of 3D scaffolds of mesoporous bioactive glasses doped metallic silver nanoparticles by rapid prototyping (SC-MBG-xAg)

The EnvisionTEC GmbH 3D Bioplotter™ device was used for 3D scaffolds preparation by rapid prototyping (RP) technique. The injectable slurries were prepared in a one-pot synthesis using the same procedures described for the synthesis of MBG-*x*Ag (x = 0, 0.15, 0.3 and 1) materials and (hydroxypropyl)methyl cellulose (HPMC) that acts as a binder agent, as previously reported [62,63]. The sol was left to age for an adequate time before the 1.5 g of HPMC (average Mn = 86,000) were added to generate an ink with a suitable consistency to be extruded by RP technique. HPMC acted as macrostructure template and the RP technique for the creation of ultra-large macropores. The solvent evaporation favours the scaffold hardening process, so the pieces were left to dry at 30 °C for 24 h. Finally, the last step consisted of calcining the pieces in air at 700 °C for 6 h to remove the organic templates (P123 and HPMC), to eliminate nitrates and to reduce silver ions to metallic AgNPs yielding the final scaffold samples denoted SC-MBG-*x*Ag (x = 0, 0.15, 0.3 and 1). Scheme 1B includes a schematic representation of the process carried out in 3D scaffolds manufacture.

2.3. Characterization of MBG-xAg powder materials and SC-MBG-xAg scaffolds

By X-ray fluorescence spectroscopy (XRF), the chemical compositions of the samples were determined using a Philips PANalytical AXIOS spectrometer (Philips Electronics NV), with X-rays generated by the RhKα line at λ = 0.614 Å. Table 1 and Table S2 (Supporting Information) record the XRF-analyzed compositions. Thermogravimetric analyses (TG) were carried out in a dynamic air atmosphere between 30 and 900 °C (flow rate of 100 mL/min with a heating rate of 5 °C/min) using a Perkin-Elmer Diamond analyser (Perkin-Elmer, USA). The textural properties of samples were obtained by nitrogen adsorption/desorption analyses at 77K on a Micromeritics ASAP 2020 instrument (Micromeritics Co, Norcross, USA). Brunauer-Emmett-Teller (BET) method [64] was used to calculate the surface area (S_{BET}). The total pore volume (V_T) was determined from the amount of N_2 adsorbed at a relative pressure of 0.97. The average mesopore diameter was obtained from the adsorption branch of the isotherm by means of the Barret-Joyner-Halenda (BJH) method [65]. A Philips X'Pert diffractometer equipped with CuKα (40 kV, 20 mA) helped to determine the structural characteristics of the materials by X-ray diffraction (XRD). Transmission electron microscopy (TEM) was performed with a JEOL 2100 electron microscope operating at 200 kV and equipped with an Oxford Link EDX probe. TEM images were registered using a CCD camera (MultiScan model 794, Gatan). Surface and cross-sectional scanning electron microscopy (SEM-EDX) micrographs and EDX mapping coupled to SEM of the scaffolds were performed in a JEOL 6400 Microscope-Oxford Pentafet super ATW system.

2.4. Ion release assays

Ion release studies were performed in Todd Height Broot (THB) bacterial culture medium. To measure the solubility degree of the SC-MBG-*x*Ag scaffolds, they were placed on different 12-well transwell plates in contact with 2.5 mL of THB under shaking (100 rpm, 37 °C). Ca, P and Ag ion contents were evaluated by inductively coupled plasma/optical emission spectrometry (ICP/OES) with the OPTIMA 3300 DV device from Perkin Elmer (Waltham, MA, USA). The concentration of each ion was determined in two different samples measured by triplicate.

2.5. Cell culture

Cell culture tests were performed using the well-characterized mouse preosteoblastic cell line MC3T3-E1 (subclone 4, CRL-2593; ATCC, Mannassas, VA). The tested scaffolds were placed into each 12-well transwell plates (Corning, CULTEK, Madrid, Spain) after cell seeding. MC3T3-E1 cells were cultured in α-MEM (Sigma Chemical Company), containing FBS and penicillin-streptomycin, 10% and 1% respectively, at 37 °C in a humidified atmosphere of 5% CO_2.

Table 1
Textural properties derived from N_2 adsorption and XRD measurements for MBG-*x*Ag (x = 0, 0.15, 0.3 and 1) powder materials[a]. XRF measurements of powder samples[b].

Sample	S_{BET} (m^2/g)	V_T (cm^3/g)	D_P (nm)	d_{100} (nm)	a_0 (nm)	t_{wall} (nm)	XRF Composition (% wt)			
							SiO_2	CaO	P_2O_5	AgNPs
MBG	378	0.49	4.44	11.8	13.63	9.19	84.41	10.10	5.49	–
MBG-0.15Ag	364	0.45	4.29	14.0	16.17	11.88	84.96	9.80	5.10	0.14
MBG-0.3Ag	343	0.40	4.02	14.2	16.40	12.38	83.90	10.32	5.46	0.32
MBG-1Ag	292	0.33	3.74	12.8	14.78	11.04	83.84	9.86	5.29	1.01

[a] S_{BET} is the total surface area determined by Brunauer-Emmett-Teller (BET) method. V_T is the total pore volume obtained using the t-plot method. D_P is the pore diameter calculated by means of the Barrett-Joyner-Halenda (BJH) method from the desorption branch of N_2 isotherm. d_{100} is the d-spacing of the 100 diffraction. a_0 is the unit cell parameter calculated by XRD, being $a_0 = 2 \cdot d_{100}/\sqrt{3}$ and t_{wall} is the wall thickness calculated using the equation $t_{wall} = a_0 - D_P$ for hexagonal *p6mm* structures.
[b] The percentages in weight of SiO_2, CaO, P_2O_5 and silver nanoparticles of powder samples determined by XRF measurements.

2.5.1. Cell proliferation and cell morphology

Pre-osteoblastic MC3T3-E1 cells were indirect plated onto the different 12 well-plates at a density of 10^4 cells/mL. The different scaffolds, SC-MBG-*x*Ag (x = 0, 0.15, 0.3 and 1), were plated on the transwells and cultured for 1 and 3 days at 37 °C in a humidified atmosphere of 5% CO_2. Cell growth was analyzed using MTS (3-(4,5-dimethylthiazol-2-yl)-5-(3-carboxymethoxyphenyl)-2-(4-sulfophenyl)-2H-tetrazolium) assay. The MTS reduction assay was performed using a commercial assay and following the manufacturer's protocol (Cell-Titer Aqueous One Solution Cell Proliferation Assay). The absorbance at 490 nm was measured in a Unicam UV-500 UV–visible spectrophotometer (Thermo Spectronic, Cambridge, UK).

After 2 days of incubation in the same assay conditions, an inverted optical microscope Eclipse TS100 (Nikon) was used to evaluate cell morphology.

2.6. Bacterial assays: evaluation of antimicrobial effects

Staphylococcus aureus (ATCC 29213) and *Escherichia coli* (ATCC 25922) were used as Gram-positive and Gram-negative bacterial models, respectively. Bacteria culture was carried out by inoculation in Todd Hewitt Broth medium (THB; Sigma-Aldrich) and incubated at 37 °C with orbital shaking (100 rpm) to obtain an adequate concentration. A visible spectrophotometer (Photoanalizer D-105, Dinko instruments) was used for the determination of the working bacteria concentration.

*2.6.1. Agar disk-diffusion tests of MBG-*xAg

Agar disk diffusion tests (ADT) were used to examine the antibacterial effect of AgNPs embedded in the MBG matrices in presence of *S. aureus* and *E. coli* strains. To carry out ADT, 100 mg of each MBG-*x*Ag powder sample was compacted into disks of 10 mm diameter and 2 mm height by using uniaxial pressure at 2–4 MPa. Prior to adhesion assay, all samples were sterilized by UV irradiation for 5–10 min on each side of the disk. The solid agar surface in Petri dishes was inoculated with a *S. aureus* or *E. coli* bacterial culture suspension (1×10^{10} bacteria/mL concentration). Then, the MBG-*x*Ag disks were placed on the bacteria inoculated agar plates and incubated during 24 h at 37 °C. After that, the bacterial inhibition zone size was measured as (outer diameter of the inhibition zone - disk diameter)/2. Each study was performed in triplicate.

2.6.2. Planktonic growth inhibition tests

SC-MBG-*x*Ag (x = 0, 0.15, 0.3 and 1) sterilized scaffolds by UV irradiation for 5–10 min on each side were put in contact with 3 mL of 2×10^8 bacteria/mL *S. aureus* or *E. coli* strains in a 12-well transwell plates. 6 or 24 h later, aliquots (20 µL) were extracted and seeded in agar plates. After 24 h of culture at 37 °C in statics conditions, the colony forming units (CFUs) were counted to know how the presence of AgNPs affects the bacterial growth.

2.6.3. Biofilm degradation

S. aureus and *E. coli* biofilms were pre-developed onto round cover glasses by placing them into 24-well plates (Corning, CULTEK, Madrid, Spain) and adding 1 mL of a bacteria suspension (2×10^8 bacteria/mL) in THB medium supplemented with sucrose (4%) at 37 °C to promote the robust biofilm formation. The *S. aureus* biofilm was already formed after 24 h. The glass slides with *E. coli* were retained 48 h at 37 °C and orbital stirring replacing and renewed with 0.5 mL of fresh medium after the first 24 h. Pre-formed biofilms were placed in a 12 transwell plates and put indirectly in contact with different type of scaffolds. After 24 h of culture at 37 °C and 100 rpm of stirring conditions, the biofilms were extracted and stained with live and dead BacLigth bacteria viability kit (Thermo Fisher Scientific, Invitrogen™). Alive bacteria were stained in green (SYTO 9), dead bacteria in red (propidium iodide, PI) and calcofluor for extracellular matrix in blue. Moreover, aliquots were extracted (20 µL) and seeded in agar plates. After 24 h of culture in statics conditions and 37 °C, the colony forming units (CFUs) were counted.

2.7. MC3T3-E1 pre-osteoblastic cells and S. aureus *bacteria co-culture assay*

Since multifunctional 3D systems involve both antibacterial effect and bone regeneration processes, the need for a realistic *in vitro* test system highly representative *in vivo* condition is a very interesting approach before carrying out any *in vivo* assays. Here, we have established an *in vitro* bacteria/bone cells co-culture model system to evaluate these SC-MBG-*x*Ag (x = 0, 0.15, 0.3 and 1) scaffolds for the prevention and treatment of bone infection.

A preliminary, co-culture assays was carried out by seeding 2.5×10^5 MC3T3-E1 cells/mL (a murine calvaria-derived pre-osteoblastic cell line used as an archetypal model of *in vitro* osteogenesis [66]) for 3 h and then mixed with 10^8 bacteria/mL of *S. aureus* on well plate disk mimicking an infectious process. Todd Height Broot (THB) and complete medium (Dulbecco's Modified Eagle's Medium (α-DMEM, Sigma Chemical Company, St. Louis, MO, USA) with 10% fetal bovine serum (FBS, Gibco, BRL), 1 mM L-glutamine were used, under a CO_2 (5%) atmosphere at 37 °C for 12 h. After that, scaffolds were soaked in 12 plate transwells (Corning™ Transwell™ multiple well plate with permeable polycarbonate membrane inserts) during 24 h. Co-cultive cells were fixed with methanol for 5 min. Then, cell nuclei were stained with 3 μM 4'-6-diamino-20-phenylindole dihydrochloride (DAPI) in methanol. Afterwards, the glass disks were marked with acridine orange (AO) (BD, Franklin Lakes, New Jersey) for 20 min.,

and then washed with sterile water (to get rid of excess colouring agent). AO stains bacterial cells bright orange, while eukaryotic cells take on a subtle greenish-orange colour [67]. Glass disks were extracted to the well plate and evaluated by Fluorescence microscopy in an EVOS FL Cell Imaging System (Waltham, MA, USA) equipped with tree Led Lights Cubes (λ_{Ex} (nm); λ_{Em} (nm): DAPI (357/44; 447/60), RFP (531/40; 593/40) from AMG (Advance Microscopy Group, Bothell, WA, USA).

2.8. Statistical analysis

Results were expressed as the mean SEM (standard error of the mean) of 6 samples divided in two independent experiments (3 separate groups of samples in each one). Statistical study was achieved with the nonparametric Kruskal-Wallis test and post-hoc Dunnś test. A value of $p < 0.05$ or 0.01 was considered significant.

3. Results and discussion

3.1. Powder mesoporous materials (MBG-xAg)

Ag/MBG nanocomposites, named MBG-*x*Ag (x = 0, 0.15, 0.3 and 1), are powder mesoporous materials that are formed by mesoporous bioactive glass (MBGs) matrices with metallic silver nanoparticles (AgNPs) homogeneously embedded inside the matrices. The MBG matrices were based on the ternary system SiO_2-CaO-P_2O_5 with 85%, 10% and 5% for SiO_2, CaO and P_2O_5 nominal composition, respectively. The molar composition studied for the AgNPs was 0.15%, 0.30% and 1.0%. Thus, in this way MBG-*x*Ag were easily prepared in alcoholic medium in acidic environment by using a non-ionic surfactant Pluronic P123 as structure-directing agent and evaporation induced self-assembly (EISA) method. TEOS, TEP, $Ca(NO_3)_2{\cdot}4H_2O$ and $AgNO_3$ were used as SiO_2, P_2O_5, CaO and AgNPs sources, respectively. The last synthesis step was the calcination at high temperatures (700 °C) where the organic matter (surfactant) was removed, the MBG matrices were formed and the silver species were spontaneously reduced to metallic silver nanoparticles [68–70]. Scheme 1A summarises synthesis strategy for MBG-*x*Ag as a powder materials followed in the present work. The novelty of these Ag/MBG nanocomposites is their one-pot easy synthesis where both intrinsic properties associated with MBG matrices and AgNPs, are combined, respectively. On the one hand, these Ag/MBG nanocomposites are bioactive materials due to the high solubility of the MBG matrices, because they are capable of releasing calcium and phosphorus ions into the environment that, in contact with biological fluids, generate apatite favouring bone regeneration processes. In addition, the presence of AgNPs (well-known antibacterial agent) embedded in the MBG matrices reduces the risk of infection associated to bone regeneration processes, favouring local release on the implantation site due to, again, high solubility of MBG.

The weight percentages of SiO_2, P_2O_5, CaO and AgNPs of the resulting MBG-*x*Ag powder materials after being calcined were confirmed by XRF measurements and the nominal and experimental compositions were in agreement (Table 1).

The structures of the pristine MBG-*x*Ag (x = 0, 0.15, 0.3 and 1) samples were analyzed by powder XRD and are showed in Fig. 1A. The low angle XRD patterns revealed that all synthesized samples exhibit ordered mesoporous arrangements (Fig. 1A(a)) with an intense diffraction maximum at 2θ in the region of 1.0–1.4°, assigned to the (100) reflection, along with a poorly resolved peaks at around 2.0 and 2.3° that can be assigned to the (111) and (200) reflections. These maxima were indexed on the basis of an ordered two-dimensional (2D) hexagonal structure (*p6mm*) [48,61,71]. The wide-angle XRD patterns (Fig. 1A(b)) displayed the presence of

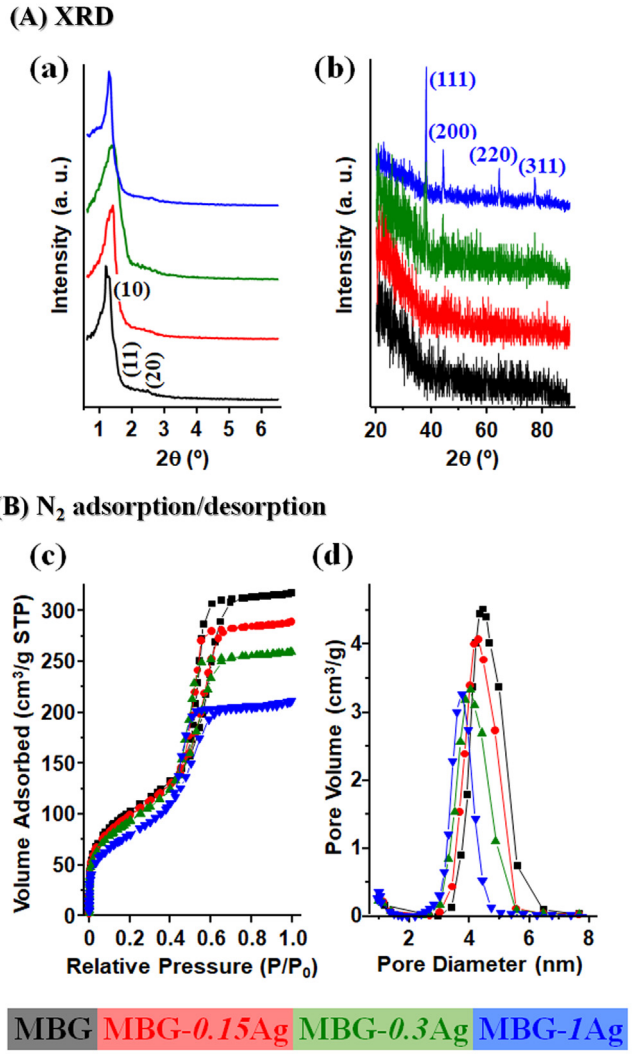

Fig. 1. **(A)** X-ray diffraction (XRD) patterns obtained for MBG-*x*Ag (x = 0, 0.15, 0.3 and 1) powder samples at low (a) and wide (b) angles. **(B)** Textural properties of MBG-*x*Ag (x = 0, 0.15, 0.3 and 1) powder samples (N_2 adsorption isotherms (c) and pore size distributions (d)) obtained by N_2 adsorption–desorption measurements.

crystalline metallic silver phase within the amorphous MBG matrix. In this way, sample containing higher amount of AgNPs (MBG-*1*Ag) displayed four well defined diffraction maxima centered at 2θ = 38.1, 44.3, 64.5 and 77.1° that can be indexed to (111), (200), (220) and (311) reflections, respectively and which are attributed to face centred cubic (fcc) silver nanoparticles (JCPDs card No. 04-0783) [72–75]. No peaks from other phases were detected, indicating high purity of the silver particles. The presence of these diffraction maxima in MBG-*0.3*Ag sample was detected but when the amount of silver was reduced (MBG-0.15Ag sample) the XRD technique did not have enough resolution to detect the presence of AgNPs. However, this was confirmed by other techniques such as XRF or TEM.

Textural properties revealed a significant decrease in both, surface area and pore volume, with the metallic AgNPs doping. All the isotherms, according to the IUPAC classification, can be identified as typical type IV which are characteristic of mesoporous solids [71,76]. The presence of H1 type hysteresis loops in the mesoporo range indicated the existence of open ended cylindrical mesopores with narrow pore size distributions, which are characteristic of MBGs [65,77] in accordance with the presence of MBG acting as matrices of AgNPs support. Surface areas, pore volumes and pore

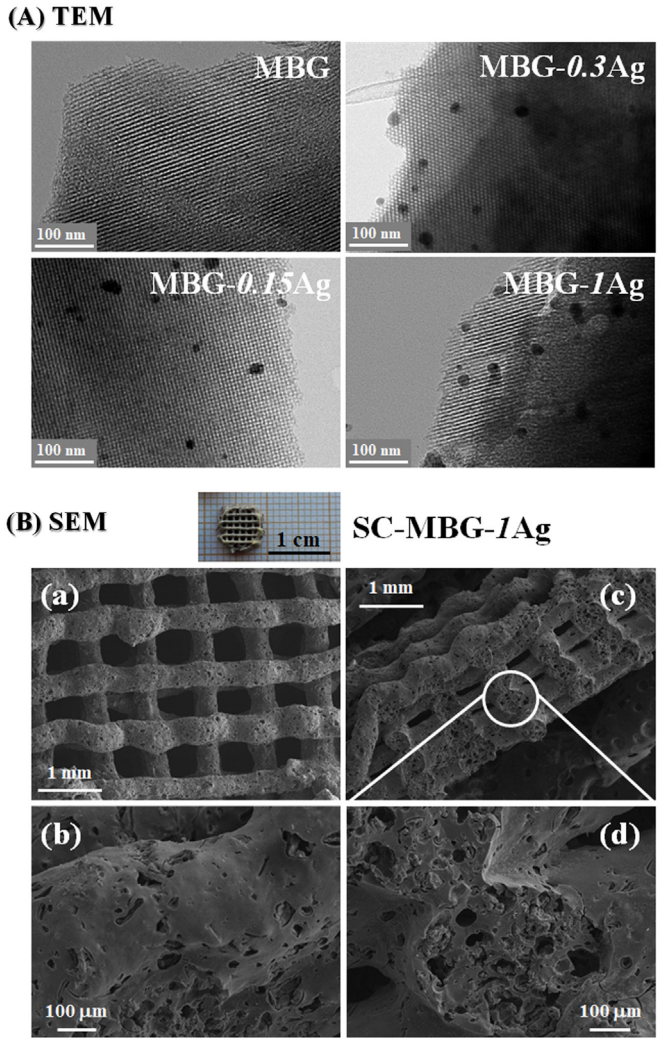

Fig. 2. **(A)** TEM images of MBG-*x*Ag (x = 0, 0.15, 0.3 and 1) powder samples. **(B)** SEM micrograph of the SC-MBG-*1*Ag sample (a) with the corresponding high-magnification image (b) and the cross-section (c), where macropores caused by HPMC removal can be observed and the corresponding high-magnification image (d).

diameters displayed a progressive decrease with increasing silver content, probably caused by blockage of the mesostructure assembly, although partial pore blockage cannot be ruled out.

The mesostructure of MBG matrices and distribution and morphology of silver particles in the MBG-*x*Ag (x = 0.15, 0.3 and 1) materials were investigated by TEM. According to low angle XRD patterns, all TEM images (Fig. 2A) displayed electron beams parallel and perpendicular to the mesoporous channels axis, showed "well ordered" hexagonally arranged mesostructures corresponding to the presence, in all samples, a very ordered MBG matrices. Regardless silver content the high ordered mesoporosity is not affected. In addition, nevertheless of the silver content, MBG-*x*Ag (x = 0.15, 0.3 and 1) nanocomposites display homogeneously distributed AgNPs (dark spots). The size of the AgNPs is rather uniform with quasi-spherical morphologies and diameters ranging from 10 to 30 nm. The AgNPs exceed the pore diameter of the MBG matrix channels, which leads to the conclusion that most AgNPs are located outside the MBG pores, thus not deforming them. These results demonstrate that the AgNPs are embedded into the MBG matrix, allowing the formation of the mesostructure during the synthesis procedure and carbonization treatment. When the silver content increased (data not included in this work) the formation of silver aggregates were observed, and their distribution into the MBG matrix loosed uniformity and homogeneity. In these cases the periodicity of the MBG matrix structures were modified and worm-like structures were obtained.

In order to investigate the effect of the silver content on the textural properties of the MBG-*x*Ag nanocomposites, N_2 adsorption/desorption measurements were done (Table 1 and Fig. 1B). Textural properties revealed a significant decrease in both, surface area and pore volume, with the metallic AgNPs doping. All the isotherms, according to the IUPAC classification, can be identified as typical type IV which are characteristic of mesoporous solids [71,76]. The presence of H1 type hysteresis loops in the mesoporo range indicated the existence of open ended cylindrical mesopores with narrow pore size distributions, which are characteristic of MBGs [65,77] in accordance with the presence of MBG acting as matrices of AgNPs support. Surface areas, pore volumes and pore diameters displayed a progressive decrease with increasing silver content, probably caused by blockage of the mesostructure assembly, although partial pore blockage cannot be ruled out.

3.2. Three-dimensional scaffolds (SC-MBG-xAg)

The hierarchical meso-macroporosity of 3D printed scaffolds plays a key role in the biological functions after implantation in bone. A proper hierarchical structure and appropriate surface chemistry and topography favour the process of cell attachment, proliferation and differentiation, as 3D scaffolds act as temporary templates for bone tissue regeneration ensuring complete cell colonization. The Ag/MBG nanocomposites manufactured as 3D scaffolds (described here) have been synthesized directly in a unique step using novel and innovative methodology: sol-gel method, which is employed to obtain AgNPs-doped MBG matrices in which different polymeric templates facilitate the diverse size scales presence, and rapid prototyping (RP) technique that provides ultra-large macroporosity according to computer-aided design. In all synthesis cases, calcination is required, not only to remove organic material (generating meso and macroporosity) and to form homogenous metallic AgNPs (by reducing silver species) embedded in the MBG matrices. Scheme 1B summarizes the manufacture of the final 3D scaffolds. Thus, in a more detail, 3D scaffolds based on Ag/MBG nanocomposite (SC-MBG-*x*Ag, x = 0, 0.15, 0.3 and 1) were prepared by RP technique via direct-write assembly of precursor slurries with adequate properties that allow their robotic printing. The employed slurries came from a sol synthesized by means of a hydroalcoholic solution of a surfactant together with the corresponding inorganic precursors, suitable aging and the subsequent addition of (hydroxypropyl)methyl cellulose (HPMC). It is essential to control the formation of the mesophase before the HPMC addition because this biomacromolecular polymer could disrupt the formation of an ordered mesostructure. Thus, before the addition of HPMC an aging stage is required to ensure the formation of an ordered mesostructure. Consequently, HPMC is added after evaporation of approximately three quarters of the sol volume. So, HPMC was added to the sol after the appropriate aging time for two purposes: (i) to increase the viscosity of the sol, resulting in slurries that could be extruded by RP; and (ii) to act as porogen, resulting in the formation of macropores after its removal by calcination [62,63]. It cannot be forgotten that the silver species were spontaneously reduced to metallic AgNPs during calcination process, so the calcination is a key step synthesis and scaffold forming of these materials. Thus the MBGs acting as a building block to confine and enclose the AgNPs. Scheme 1 (right bottom) displays a digital photograph of cylindrical scaffolds before and after calcination process and without (white) or with (brown) AgNPs presence in their composition. In addition, thermogravimetric (TG) analysis indicated that 700 °C is a suitable temperature not only for the silver species

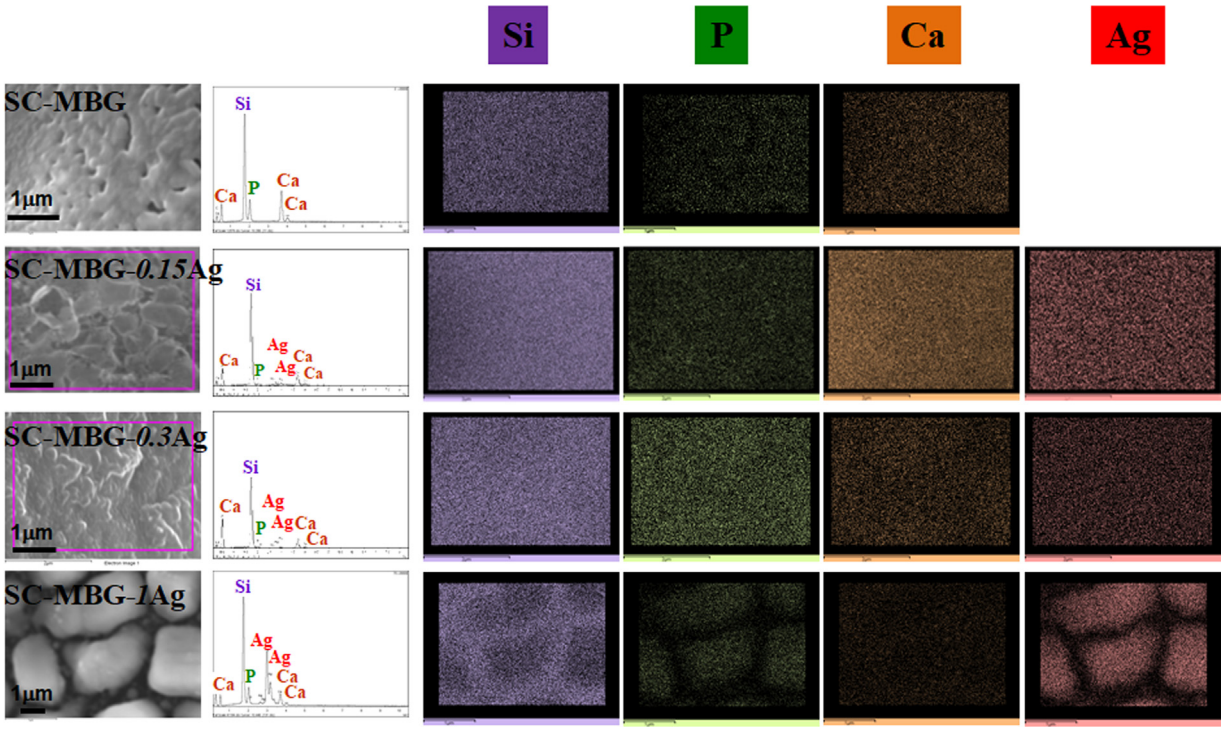

Fig. 3. SEM images, EDS spectra and Si, P, Ca and Ag elements distribution of SC-MBG-*x*Ag (x = 0, 0.15, 0.3 and 1) scaffolds.

reduction to AgNPs but also for the elimination of organic matter, nitrate groups and HPMC (necessary for the scaffolds manufacture by RP technique). The results obtained by TG measurements (Fig. S1, Supporting Information) revealed that there were slightly different weight losses between materials with and without AgNPs presence that were in accordance with the XRF results (Table S2). Thus, the successful doped with AgNPs on the mesoporous matrices has been confirmed.

Fig. 2B shows SEM images of SC-MBG-*1*Ag scaffold, selected as a representative example. SEM micrographs show a stacked rod lattice with simple tetragonal symmetry as a result computer-aided design by RP technique. The rods width is *ca.* 350 μm and the ultra-large pores present sizes of *ca.* 450 μm, as depicted in Fig. 2B(a) (frontal view) and 2B(c) (cross view). This ultra-large porosity of *ca.* 400 μm is in agreement with the porosity required for regenerating bone tissues, as reported by several authors [78,79]. SEM micrograph at higher magnification (Figure 2B(b)) shows that this scaffold is formed by cylinders with relatively smooth surfaces. However, a SEM micrograph of the cross-section of this scaffold showed the presence of heterogeneous macropores, with sizes ranging from 20 to 60 μm (Fig. 2B(b) and 2B(d)), which were results of the HPMC removal by calcination process generating macroporous systems with high interconnection.

Energy-dispersive spectrometry analysis (EDS) mapping analysis took place and the results are displayed in Fig. 3. Quantitative analysis using EDS mapping, coupled to SEM, was used to explore the Si, P, Ca and Ag elements distribution in the SC-MBG-*x*Ag scaffolds. Micrographs showed that Si, P, Ca and Ag elements were evenly and homogenously distributed in all the scaffolds.

Once the macroporous nature of the manufactured SC-MBG-*x*Ag scaffolds had been investigated, a deep study of the mesostructural structures of the different scaffold series was carried out by XRD, TEM and N_2 adsorption techniques. No mayor differences have been found between scaffolds and powder materials, although it is true that the diffraction maxima are not so well defined and the TEM micrographs showed a worse definition in the arrangement of the mesopore channels. The XRD pattern showed peaks that can be indexed as reflections that correspond to the 2D hexagonal structure with *p6mm* space group. The AgNPs presence was also confirmed by wide angle XRD patterns and TEM images (difractograms and micrographs are included in the Supplementary Material, Fig. S2). We can conclude that the shaping of materials in scaffolding forms thanks to HPMC inclusion does not affect AgNPs morphologies nor their homogeneous distribution within the MBG matrices, although the MBG matrices lost part of mesostructure observed for the powder materials.

The textural properties of scaffolds resulting from the appropriate treatment of N_2 adsorption were slightly affected by manufacture scaffold procedure and are summarized in Table S2 (Supplementary Material). Surface area, pore volume and pore diameter values decreased with respect to the values found for powder samples. In any case, all scaffold samples showed a similar behaviour that was in agreement with previously reported observations to powder materials. AgNPs incorporation into the mesoporous MBG network usually led to a decrease in the textural properties that could be attributed of the partial collapse of the pore structure of MBG matrices due to HPMC incorporation during the synthesis process. But in no case their mesoporosity were compromised because the scaffold samples displayed high pore volumes and specific surface areas [53,54,62,63,80-82]. The sum of macropore and mesopore interconnections from MBG matrices will promote the substrates diffusion within the scaffold in biological applications that require the exchange of liquids within these porous matrices.

As can be seen in Table S2 (XRF measurements, Supporting Material), the molar composition of the different scaffolds were very close to the nominal ratio which means the chemical composition were not affected by the scaffolding method.

3.3. Ion release assays

ICP-OES was used to evaluate the ions release and Fig. 4 displays the results obtained. The medium chosen for the ion release study was bacteria culture medium (THB) due to the purpose of these materials is to be used for infection treatment. These mate-

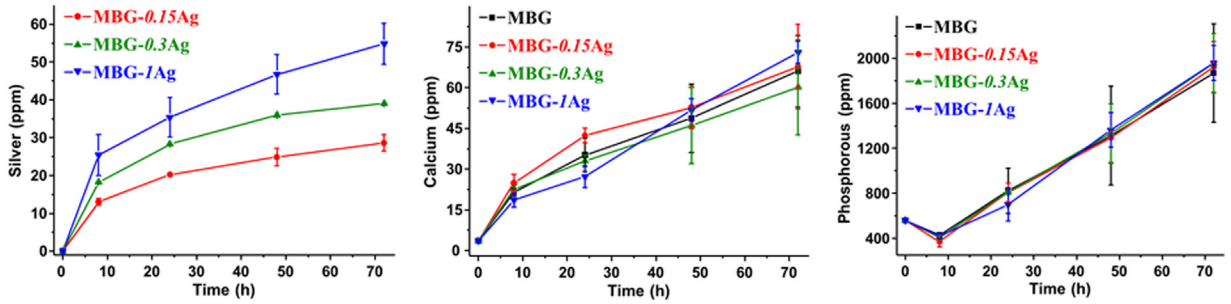

Fig. 4. Evolution of cumulative calcium, phosphorus, and silver content SC-MBG-*x*Ag (x = 0, 0.15, 0.3 and 1) scaffolds as a function of time in THB medium.

rials displayed a high *in vitro* ions release capabilities due to the open interconnected meso-macroporosity of the scaffolds that facilitate the release of ions to the media. This hierarchical porosity, present in the 3D scaffolds, with high surface area property facilitate an adequate interaction with biological fluids necessary to favour their solubility. Due to the one-step synthesis process, the Ag concentrations in the assembly procedure adjust the loading of Ag nanospecies into the hierarchically structured silica and result in similarly sized and homogeneously distributed nanoparticles. In addition, AgNPs indicate that it facilitates the solubility of the samples because the calcium and phosphorus release profiles were higher than those of the scaffolds without silver were. In any case, samples exhibited analogous calcium and phosphorous release behaviours with under-went a sustained increase with time as expected to MBG matrices, that are in accordance with systems with high bioactivity [53,54,62,63,80,81]. It has been observed that there was a direct relationship between silver molar composition and silver release to THB medium. Sample with the highest amount of silver, SC-MBG-*1*Ag, released the highest amount of ppm to the medium while the SC-MBG-*0.15*Ag and SC-MBG-*0.3*Ag profiles were very similar. The antibacterial activity of metallic silver is directly related to the release of Ag^+ ions, for which an oxidation of Ag(0) to Ag(I) takes place in aqueous solution, with the presence of oxygen and under acidic conditions [83–85].

$$4\ Ag + O_2 \rightarrow 2\ Ag_2O \quad (1)$$

$$2\ Ag_2O + 4H^+ \rightarrow 4\ Ag^+ + 2\ H_2O \quad (2)$$

We have observed that for all the materials studied (SC-MBG-*x*Ag, x = 0.15, 0.3 and 1), the Ag^+ release after three days is around ≈15–20 ppm, and it is appropriate to display antibactericidal activity in *S. aureus* and *E. coli* bacteria [34].

Taking into account that THB contains calcium and phosphorus in its composition and MBG matrices also contain, SC-MBG-*x*Ag displayed the typical of highly bioactive glasses profiles: a very fast calcium and phosphorous release at short times followed by precipitation equilibrium due to the formation of apatite-type calcium phosphates, indicating that these materials exhibit bioactive behaviour. External surface of SC-MBG-*x*Ag were evaluated after 10 days in THB incubation by wide-angle XRD (Figure S3). In addition to the maxima corresponding to the presence of AgNPs, new maxima can be observed in all samples. These new specimens are assigned to the newly formed apatite, confirming that all these materials exhibit excellent bioactive properties.

3.4. In vitro *assays: MC3T3-E1 preosteoblastic cells culture of 3D scaffolds*

To evaluate whether the presence of metallic AgNPs contributes to the cytotoxicity of SC-MBG-*x*Ag materials, these scaffolds were placed by indirect contact with MC3T3-E1 preosteoblastic cells under transwell plates and their cell growth was studied by MTS assays. Fig. 5 shows the results obtained of cell viability assays after 1 and 3 days of incubation. It can be seen that at short times all materials showed similar viability. After 3 days of culture, cell growth increased considerably for all scaffolds, with and without AgNPs.

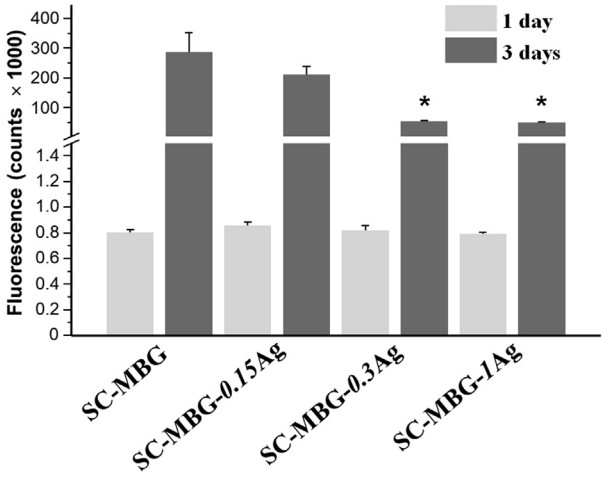

Fig. 5. MTS proliferation assay of MC3T3-E1 preosteoblastic cells in the presence of SC-MBG-*x*Ag (x = 0, 0.15, 0.3 and 1) scaffolds after 1 and 3 days of incubation. Controls correspond to cells incubated in the absence of scaffolds. Results are mean ± SE (n = 3). $^*p < 0.05$ SC-MBG *vs* the corresponding SC-MBG-*x*Ag (x = 0.3 and 1).

MTS assays showed that the number of live cells in cultures was affected by the presence of AgNPs in the MBG matrices due to the cell viability decreased with increasing presence of metallic AgNPs. MC3T3-E1 cell growth test revealed that those materials with a higher silver content (x = 0.3 and 1) presented increase more slowly than SC-MBG-*x*Ag (x = 0 and 0.15). Although we can conclude that in all cases all scaffolds SC-MBG-*x*Ag (x = 0.15, 0.3 and 1) were no cytotoxic and MC3T3-E1 cells proliferated in presence of these materials.

Moreover, MC3T3-E1 cell morphologies were evaluated by the optical microscope and representative images were included in Figure S4 (Supplementary Material). In all cases, the MC3T3-E1 cells maintained their typical osteoblast morphology and they were totally spread on the plastic plate after two days of incubation in contact with SC-MBG-*x*Ag (x = 0 and 0.15, 0.3 and 1), so their morphology and viability were not affected.

3.5. *Antibacterial properties evaluation of Ag/MBG nanocomposites*

In order to evaluate the antibacterial properties of Ag/MBG nanocomposites as a powder materials or 3D scaffolds, *in vitro*

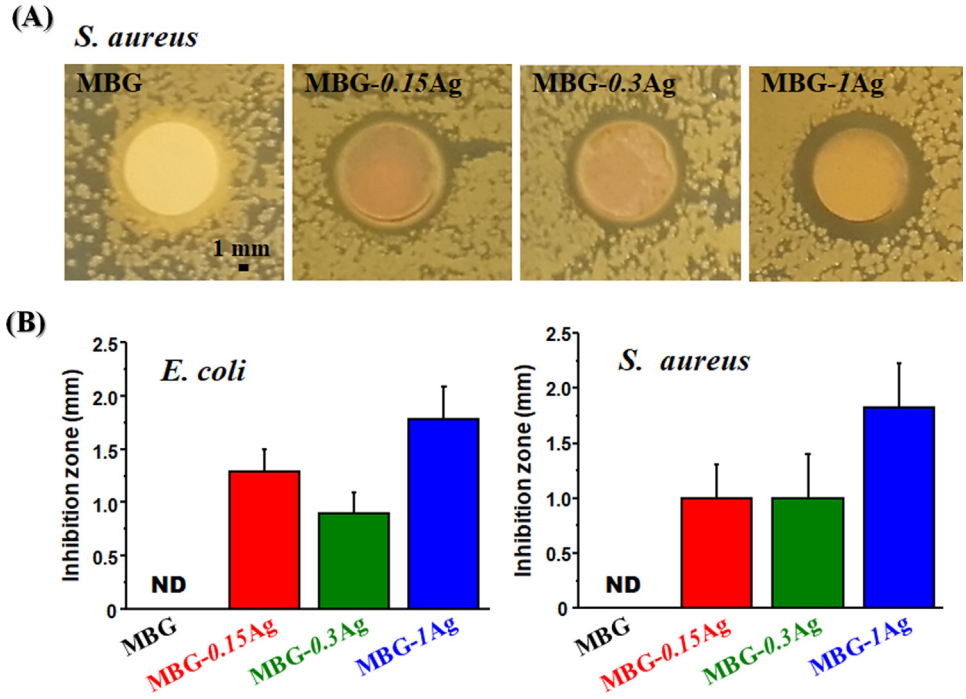

Fig. 6. **(A)** Digital photographs of halo inhibition zones and **(B)** graphical representation of inhibition zones measurements of MBG-*x*Ag (x = 0, 0.15, 0.3 and 1) powder samples conformed as 10 mm diameter disks. Results are mean ± SE (n = 3). $^{*}p < 0.05$ control *vs* the corresponding MBG-*x*Ag (x = 0.15 and 0.3).

assays with *Staphylococcus aureus* or *Escherichia coli* strains were performed. *S. aureus* and *E. coli* were chosen as models of Gram-negative and Gram-positive bacteria, respectively, because they are responsible for more than 80 % of all infections [86,87].

The antibacterial activity of MBG-*x*Ag (x = 0, 0.15, 0.3 and 1) powder samples were examined by agar disk diffusion tests, where *ca.* 100 mg of each powder samples were compacted into 10 mm diameter disks. Fig. 6A displays the images of inhibition halos obtained by the agar diffusion method for MBG-*x*Ag materials against *S. aureus* and Fig. 6B shows the graphs of the inhibition zones measurements against *S. aureus* and *E. coli* growth. The silver ions diffused and growth inhibition was verified by the presence of a detectable clear zone around the disks. The presence of metallic AgNPs is a prerequisite for these materials to have antibacterial activity, and it was observed that this activity is higher in both strains when the percentage of silver is higher in the composition of these powder materials, i.e. x = 1. The diameters of the inhibition zones for MBG-*1*Ag material was 1.78 and 1.83 mm for *E. coli* and *S. aureus* bacteria, respectively after 24 h.

To detect the antibacterial capacity of the 3D scaffolds, SC-MBG-*x*Ag, x = 0, 0.15, 0.3 and 1 samples were placed in different transwells and 3 mL of *S. aureus* or *E. coli* bacteria suspension (2×10^8 bacteria/mL) were added to a culture well plates. 6 and 24 h later, aliquots (20 μL) were extracted and were seeded in agar Petri plates. After 24 h of culture at 37 °C in static conditions, colony-forming units (CFUs) were counted. Controls correspond to bacteria incubated in the absence of scaffolds. Fig. 7 summarized the results obtained and undoped SC-MBG scaffolds and silver doped SC-MBG-*x*Ag (x = 0.15, 0.3 and 1) scaffolds were compared. In all cases, at 6 and 24 h and for both bacteria strains, scaffolds containing AgNPs in their composition have high antibacterial activity inhibiting the formation of bacterial colonies regardless of the molar composition of silver. It can be observed that, under these experimental conditions, AgNPs were exclusive responsible of antimicrobial effects of these nanocomposite materials even with only 0.15 molar ratio composition.

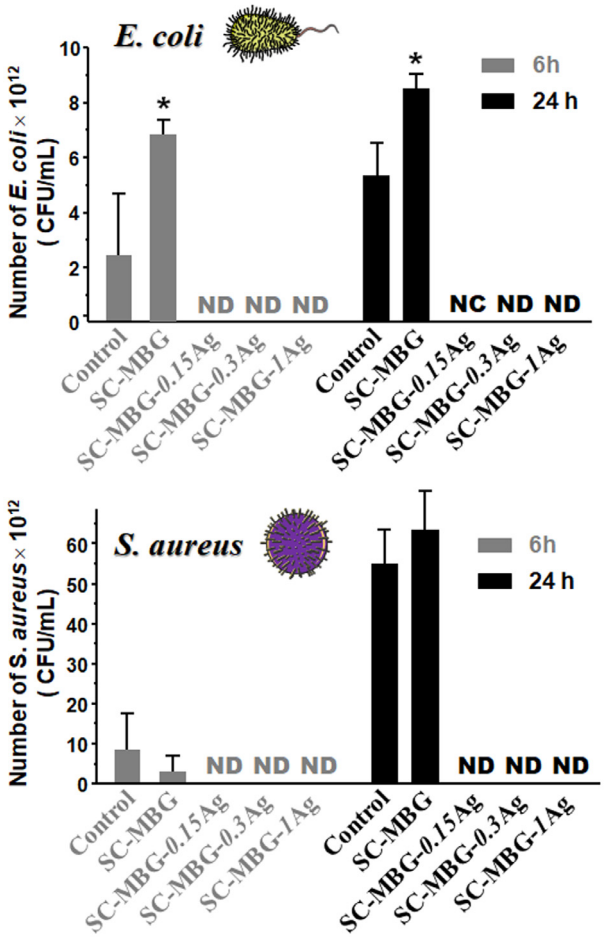

Fig. 7. Couting of colony forming units of *E. coli* and *S. aureus* after 6 and 24 h of culture in contact through a transwell with SC-MBG-*x*Ag (x = 0, 0.15, 0.3 and 1) scaffolds. Results are mean ± SE (n = 3). $^{*}p < 0.05$ control *vs* SC-MBG.

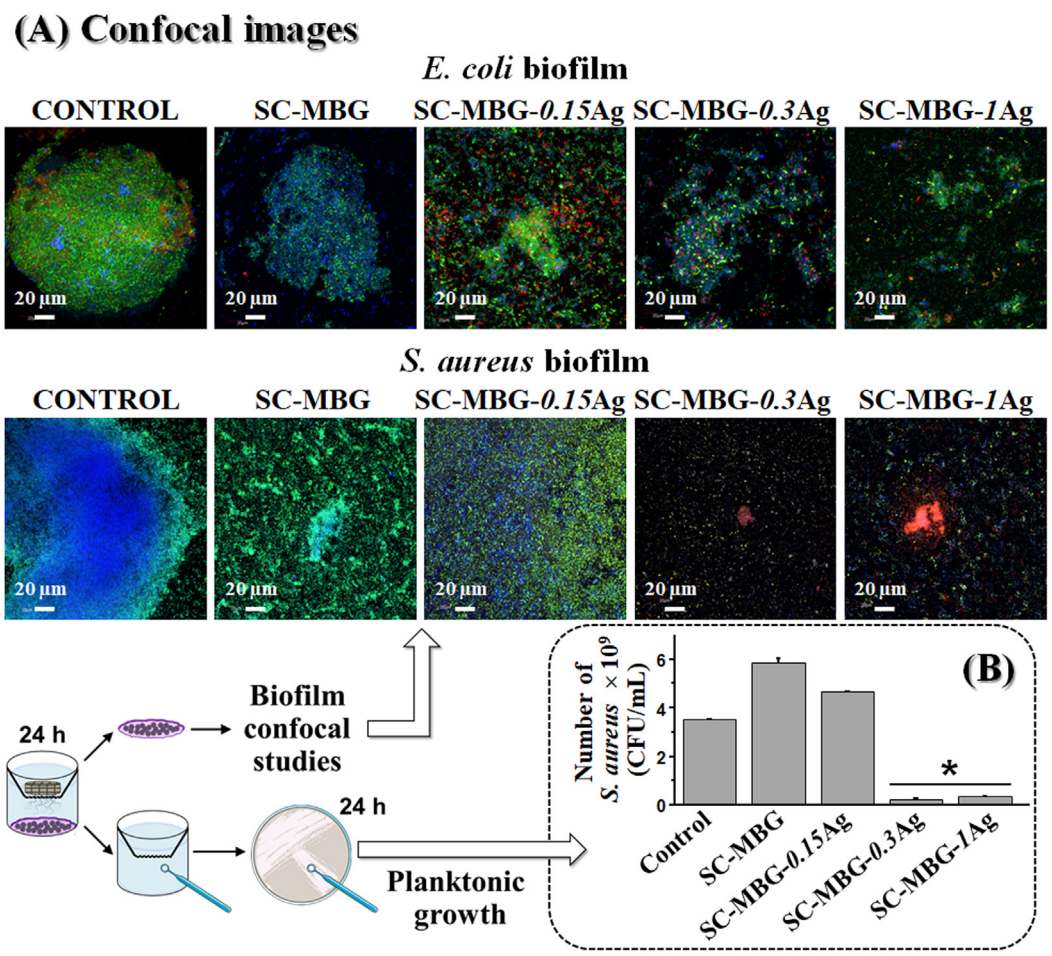

Fig. 8. **(A)** Confocal images of *E. coli* and *S. aureus* biofilm degradation after 24 h in contact through a transwell with SC-MBG-*x*Ag (x = 0, 0.15, 0.3 and 1) scaffolds. Controls correspond to biofilms incubated in the absence of scaffolds. Live bacteria were stained in green, dead bacteria in red and the protective extracellular polysaccharide matrix biofilm in blue. **(B)** Couting of colony forming units of *S. aureus* after 24 h of culture of aliquots that were extracted after previously contact of *S. aureus* with SC-MBG-*x*Ag (x = 0, 0.15, 0.3 and 1) scaffolds during 24 h. Statistical significance respect to SC-MBG: $^{*}p < 0.01$.

Although the incorporation the incorporation of multivalent ions (Mg, Zn, B, Ga, Zn, Ag) to the SiO_2–CaO–P_2O_5 system of MBG reduces the specific surface area and pore volume, it has no distinct effect on the pore size and the resultant ceramics still possessed a high surface area and pore volume [88–91]. This property along with big channels and macroporosity of scaffolds contributes to more effective and homogeneous release of silver ions from the glass structure.

Confocal microscope studies were done to evaluate the silver presence effect of SC-MBG-*x*Ag (x = 0, 0.15, 0.3 and 1) scaffolds onto preformed *E. coli* and *S. aureus* biofilms (Fig. 8A). The control biofilms showed a typical structure composed by a mat of live bacteria (green) covered with a protective polysaccharide layer (blue). Biofilms incubated for 24 h with undoped metallic AgNPs scaffolds (SC-MBG) displayed similar structure than control biofilms, where green and blue colours assigned to live bacteria and protective extracellular polysaccharide matrix predominated. For biofilms incubated with Ag doped scaffolds (SC-MBG-*x*Ag, x = 0.15, 0.3 and 1), a remarkable reduction of the biofilm area was observed, together with the presence of dark gaps and an increase in dead bacteria (red colour) coexisting with small isolated live bacterial colonies along the entire surface. These results indicated that was necessary the AgNPs presence to cause disruption of biofilm. The differences in antimicrobial efficacy between x = 0.15, 0.3 and 1 can be attributed to the greater presence of metallic AgNPs antimicrobial effect that released Ag^{+} ions to the media and are consistent with the antimicrobial effect in the planktonic state and inhibition zone formation. The results showed that antimicrobial effect was more effective against *S. aureus* biofilm than *E. coli* biofilm.

Once tested the effect of AgNPs doping samples on *S. aureus* biofilm and with the aim to complete these antimicrobial studies, different aliquots of resulting media where seeded in agar Petri plates. After 24 h of incubation at 37 °C in static conditions, *S. aureus* colony forming units were counted (Fig. 8B). In agreement with the above results, both SC-MBG-*0.3*Ag and SC-MBG-*1*Ag samples displayed the lowest number of *S. aureus* colonies because the presence of these molar ratios of AgNPs were more effectively destroyed the previous biofilm. Therefore, these Ag/MBG nanocomposite hierarchical scaffolds exhibited, as the same time, the cytocompatible and antibacterial properties for prevention and treatment of bone infection applications.

3.6. Co-culture assays

Qualitative results of the *in vitro* co-culture assays of preosteoblastic MC3T3-E1 cells and *S. aureus* bacteria are summarized in the confocal microscope images showed in Fig. 9. The cells adhesion and spreading onto plate surfaces were visualized by fluorescence microcopy where actin cytoskeleton was stained with acridine orange (in orange) and the nuclei with DAPI (in blue). Bacterial cells were stained in a bright orange with acridine orange. When SC-MBG-*x*Ag (x = 0, 0.15, 0.3 and 1) scaffolds were put indi-

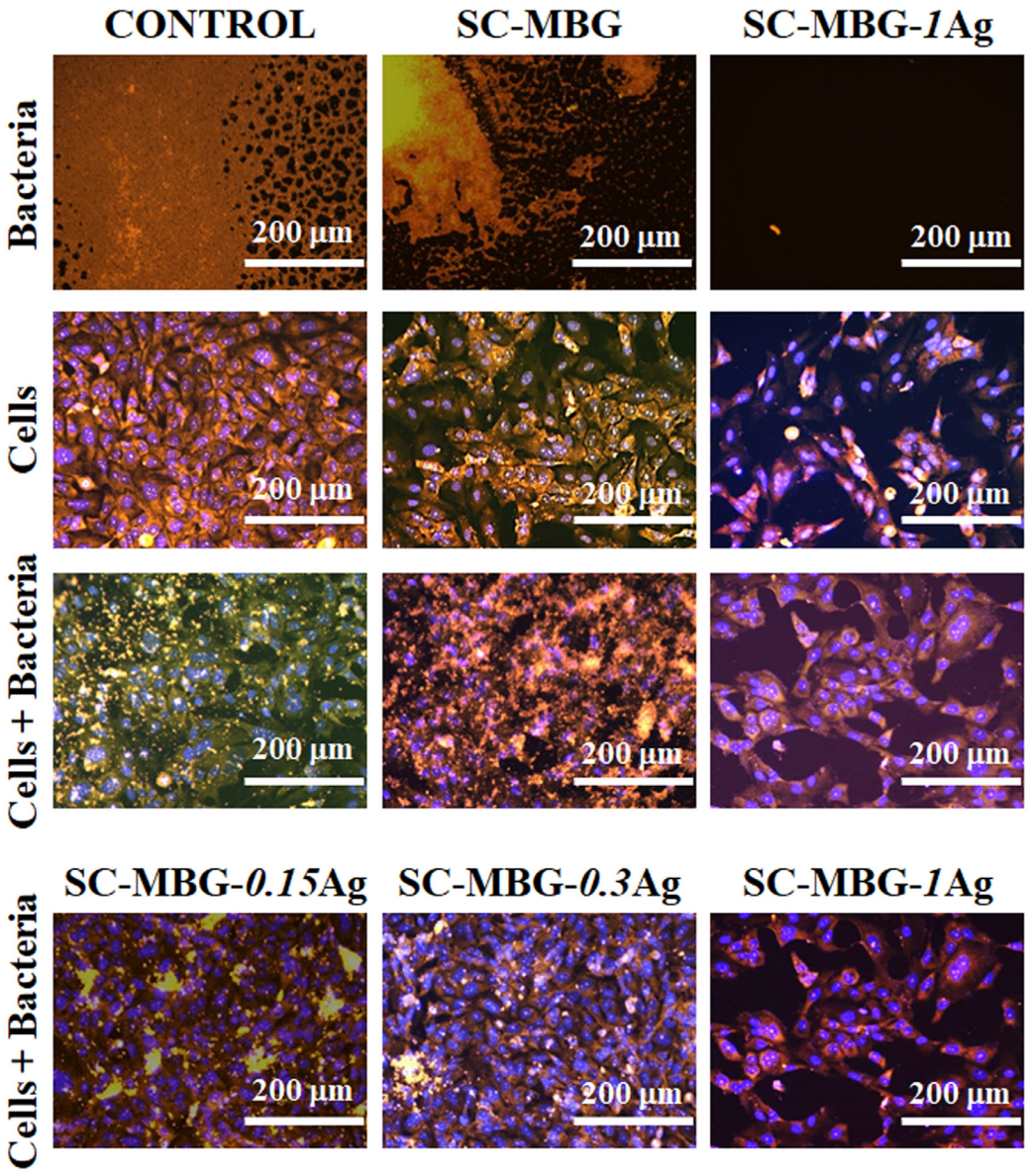

Fig. 9. Microscope images of preosteoblastic MC3T3-E1 cells and *S. aureus* bacteria co-cultured for 24 h and placed in indirect contact with SC-MBG-*x*Ag scaffolds (x = 0, 0.15, 0.3 and 1) for a further 24 h. *S. aureus* bacteria and preosteoblastic cells cytoskeleton were stained in orange and cells nuclei were stained in blue.

rect contact through a transwell during 24 h with MC3T3-E1 cells, *S. aureus* bacteria and a co-cultive of cells and bacteria we can confirmed that:

(i) Silver doping is necessary to have antibacterial activity. It could be observed that only samples with AgNPs destroyed the *S. aureus* bacteria. The presence of the orange colour, associated with the bacteria staining, was reduced when the percentage of AgNPs increases indicating that antimicrobial activity is higher the more silver the materials contain.
(ii) The images showed viable and well-spread cells which have maintained their typical preosteoblast morphology for all kind of scaffolds, with or without metallic AgNPs. A decrease in the number of cells could be observed as the percentage of silver increased, which is in agreement with the previously described results of cytotoxicity.
(iii) In assays performed with MC3T3-E1 cells and *S. aureus* bacteria co-cultured for 24 h, it was observed by microscopy imaging that the cells are hardly affected by the presence of the scaffolds whereas the number of bacteria decreases as the percentage of AgNPs increases. The qualitative results of the co-cultive followed the same pattern as the studies performed on cells or bacteria independently.

4. Conclusions

This research work highlights the versatility of the metallic doping method developed here to prepare MBGs with antibacterial properties, which could be applied depending on the targeted clinical application in different shapes as powders, particles, dense or porous supports. Dual Ag/MBG nanocomposites for bone tissue regeneration with antimicrobial activity were synthetized where AgNPs were homogeneously embedded into ordered mesoporous bioactive glasses based on the ternary system SiO_2–CaO–P_2O_5. These Ag/MBG nanocomposites were prepared in a unique synthesis step by the sol–gel method followed by EISA process with a spontaneous reduction of silver salts to AgNPs by high temperature. Their manufacture as three-dimensional scaffolds with hierarchical porosity was carried out by (hydroxypropyl)methyl cellulose

(HPMC) use, which facilitated the formation of suitable inks to be extruded by the rapid prototyping (RP) technique.

MBG matrices solubility facilitated the bioavailability of AgNPs allowing a release of silver ions into the medium, which are responsible for the antimicrobial activity of these materials. *In vitro* antimicrobial assays showed that *S. aureus* and *E. coli* growth inhibition and biofilm reduction were directly related to the increased presence of AgNPs into the MBG matrices. These amounts of AgNPs did not compromise the viability of the MC3T3-E1 preosteoblastic cells cultured with Ag/MBG nanocomposites. The results obtained in the co-culture of Ag/MBG nanocomposites with MC3T3-E1 cells and *S. aureus*, trying to simulate *in vivo* conditions in an *in vitro* environment, indicated that these materials are excellent candidates for more *in vitro* and future *in vivo* assays for the treatment of bacterial infection and bone tissue regeneration.

Declaration of Competing Interest

The authors declare no conflict of interest.

Acknowledgments

Authors acknowledge funding from the European Research Council (Advanced Grant VERDI; ERC-2015-AdG Proposal No. 694160), the Ministerio de Ciencia e Innovación through the project PID2019-106436RB-I00 and the Instituto de Salud Carlos III, grant number PI20/01384 co-financed with the European Union FEDER funds.

Supplementary materials

Supplementary material associated with this article can be found, in the online version, at doi:10.1016/j.actbio.2022.10.045.

References

[1] L.L. Hench, M.B. Fenn, J.R. Jones, New Materials and Technologies for Healthcare, World Scientific, 2012.
[2] R.O. Darouiche, Treatment of infections associated with surgical implants, N. Engl. J. Med. 350 (2004) 1422–1429.
[3] WHONew Report Calls for Urgent Action to Avert Antimicrobial Resistance Crisis, World Health Organization, 2019 Available online: https://www.who.int/news/item/29-04-2019-new-report-calls-for-urgent-action-to-avert-antimicrobial-resistance-crisis. Accessed on March 2022.
[4] WHOAntimicrobial Resistance: Global Report on Surveillance, World Health Organization, Geneva, Switzerland, 2014 2014.
[5] WHOGlobal Antimicrobial Resistance and Use Surveillance System (GLASS), World Health Organization, 2022 Available online: https://www.who.int/initiatives/glass. Accessed on March 2022.
[6] M. Vallet-Regí, Our contributions to applications of mesoporous silica nanoparticles, Acta Biomater. 137 (2022) 44–52.
[7] M. Vallet-Regí, F. Schüth, D. Lozano, M. Colilla, M. Manzano, Engineering mesoporous silica nanoparticles for drug delivery: where are we after two decades? Chem. Soc. Rev. 51 (2022) 5365–5451.
[8] R.M. Donlan, J.W. Costerton, Biofilms: Survival mechanisms of clinically relevant microorganisms, Clin. Microbiol. Rev. 15 (2002) 167–193.
[9] K. Saeed, A.C. McLaren, E.M. Schwarz, V. Antoci, W.V. Arnold, A.F. Chen, M. Clauss, V. Gant, E. Hendershot, N. Hickok, C.A. Higuera, D.C. Coraça-Huber, H. Choe, J.A. Jennings, M. Joshi, W.T. Li, P.C. Noble, K.S. Phillips, P.S. Pottinger, C. Restrepo, H. Rohde, T.P. Schaer, H. Shen, M. Smeltzer, P. Stoodley, J.C.J. Webb, E. Witsø, International consensus meeting on musculoskeletal infection: summary from the biofilm workgroup and consensus on biofilm related musculoskeletal infections, J. Orthop. Res. 37 (5) (2019) 1007–1017.
[10] M. Kanayama, T. Hashimoto, K. Shigenobu, F. Oha, A. Iwata, M. Tanaka, MRI-based decision making of implant removal in deep wound infection after instrumented lumbar fusion, Clin. Spine Surg. 30 (2) (2017) E99–E103.
[11] S. Rosas, A.C. Ong, L.T. Buller, K.G. Sabeh, T.Y. Law, M.W. Roche, V.H. Hernández, Season of the year influences infection rates following total hip arthroplasty, World J. Orthop. 8 (12) (2017) 895–901.
[12] D.W. Hutmacher, Scaffolds in tissue engineering bone and cartilage, Biomaterials 21 (2000) 2529–2543.
[13] R. Agarwal, A.J. García, Biomaterial strategies for engineering implants for enhanced osseointegration and bone repair, Adv. Drug Deliv. Rev. 94 (2015) 53–62.
[14] L. Roseti, V. Parisi, M. Petretta, C. Cavallo, G. Desando, I. Bartolotti, B. Grigolo, Scaffolds for bone tissue engineering: state of the art and new perspectives, Mater. Sci. Eng. C 78 (2017) 1246–1262.
[15] A. Wubneh, E.K. Tsekoura, C. Ayranci, H. Uludağ, Current state of fabrication technologies and materials for bone tissue engineering, Acta Biomater. 80 (15) (2018) 1–30.
[16] A. Haleem, M. Javaid, R.H. Khan, R. Suman, 3D printing applications in bone tissue engineering, J. Clin. Orthop. Trauma 11 (2020) S118–S124.
[17] A. García, M.V. Cabañas, J. Peña, S. Sánchez-Salcedo, Design of 3D scaffolds for hard tissue engineering: from apatites to silicon mesoporous materials, Pharmaceutics 13 (2022) 1981.
[18] E. Sachs, M. Cima, J. Cornie, Three-dimensional printing: Rapid tooling and prototypes directly from a CAD model, CIRP Ann. 39 (1990) 201–204.
[19] R. Petzold, H.F. Zeilhofer, W.A. Kalender, Rapid protyping technology in medicine-basics and applications, Comput. Med. Imaging. Graph. 23 (1999) 277–284.
[20] R. Landers, U. Hübner, R. Schmelzeisen, R. Mülhaupt, Rapid prototyping of scaffolds derived from thermoreversible hydrogels and tailored for applications in tissue engineering, Biomaterials 23 (2002) 4437–4447.
[21] J. Kundu, F. Pati, J.H. Shim, D.W. Cho, Rapid prototyping technology for bone regeneration, in: R. Narayan (Ed.), Rapid Prototyping of Biomaterials: Principles and Applications, Woodhead Publishing, 2014, pp. 254–284.
[22] P.S. Sapkal, S. Jaiswal, A.M. Kuthe, Rapid prototyping assisted scaffold fabrication for bone tissue regeneration, J. Mater. Sci. Res. 5 (4) (2016) 79–95.
[23] B. Yuan, S.Y. Zhou, X.S. Chen, Rapid prototyping technology and its application in bone tissue engineering, J. Zhejiang Univ. Sci. B 18 (4) (2017) 303–315.
[24] A.P. Moreno-Madrid, S.M. Vrech, M.A. Sánchez, A.P. Rodríguez, Advances in additive manufacturing for bone tissue engineering scaffolds, Mater. Sci. Eng. C 100 (2019) 631–644.
[25] S. Eckhardt, P.S. Brunetto, J. Gagnon, M. Priebe, B. Giese, K.M. Fromm, Nanobio silver: its interactions with peptides and bacteria, and its uses in medicine, Chem. Rev. 113 (2013) 4708–4754.
[26] K.M. Fromm, Silver coordination compounds with antimicrobial properties, Appl. Organomet. Chem. 27 (2013) 683–687.
[27] P. Dibrov, J. Dzioba, K.K. Gosink, C.C. Hase, Chemiosmotic mechanism of antimicrobial activity of Ag in *Vibrio cholerae*, Antimicrob. Agents Chemother. 46 (2002) 2668–2670.
[28] K. Chaloupka, Y. Malam, A.M. Seifalian, Nanosilver as a new generation of nanoproduct in biomedical applications, Trends Biochem. 28 (11) (2010) 580–588.
[29] A.G. Khina, Y.A. Krutyakov, Similarities and differences in the mechanism of antibacterial action of silver ions and nanoparticles, Appl. Biochem. Microbiol. 57 (6) (2021) 683–693.
[30] J.R. Morones, J.L. Elechiguerra, A. Camacho, K. Holt, J.B. Kouri, J.T. Ramírez, M.J. Yacaman, The bactericidal effect of silver nanoparticles, Nanotechnology 16 (10) (2005) 2346–2353.
[31] P.V. Asharani, Y.L. Wu, Z. Gong, S. Valiyaveettil, Toxicity of silver nanoparticles in zebrafish models, Nanotechnology 19 (25) (2008) 255102.
[32] C.N. Lok, C.M. Ho, R. Chen, Q.Y. He, W.Y. Yu, H. Sun, P.K. Tam, J.F. Chiu, C.M. Che, Silver nanoparticles: partial oxidation and antibacterial activities, J. Biol. Inorg. Chem. 12 (4) (2007) 527–534.
[33] M. Yamanaka, K. Hara, J. Kudo, Bactericidal actions of a silver ion solution on *Escherichia coli*, studied by energy-filtering transmission electron microscopy and proteomic analysis, Appl. Environ. Microbiol. 71 (11) (2005) 7589–7593.
[34] W.K. Jung, H.C. Koo, K.W. Kim, S. Shin, S.H. Kim, Y.H. Park, Antibacterial activity and mechanism of action of the silver ion in *Staphylococcus aureus* and *Escherichia coli*, Appl. Environ. Microbiol. 74 (7) (2008) 2171–2178.
[35] S. Shrivastava, T. Bera, A. Roy, G. Singh, P. Ramachandrarao, D. Dash, Characterization of enhanced antibacterial effects of novel silver nanoparticles, Nanotechnology 18 (22) (2007) 225103.
[36] W. Yang, C. Shen, Q. Ji, H. An, J. Wang, Q. Liu, Z. Zhang, Food storage material silver nanoparticles interfere with DNA replication fidelity and bind with DNA, Nanotechnology 20 (8) (2009) 085102.
[37] X. Yan, C. Yu, X. Zhou, J. Tang, D. Zhao, Highly ordered mesoporous bioactive glasses with superior *in vitro* bone-forming bioactivities, Angew. Chem. Int. Ed. 43 (2004) 5980–5984.
[38] H.S. Yun, S.H. Kim, D. Khang, J. Choi, H.H. Kim, M. Kang, Biomimetic component coating on 3D scaffolds using high bioactivity of mesoporous bioactive ceramics, Int. J. Nanomed. 6 (2011) 2521–2531.
[39] S. Sánchez-Salcedo, M. Colilla, I. Izquierdo-Barba, M. Vallet-Regí, Preventing bacterial adhesion on scaffolds for bone tissue engineering, Int. J. Bioprinting 2 (1) (2016) 20–34.
[40] S. Kargozar, M. Montazerian, S. Hamzehlou, H.W. Kim, F. Baino, Mesoporous bioactive glasses: promising platforms for antibacterial strategies, Acta Biomater. 81 (2018) 1–19.
[41] V. Lalzawmliana, A. Anand, M. Roy, B. Kundu, S.K. Nandi, Mesoporous bioactive glasses for bone healing and biomolecules delivery, Mater. Sci. Eng. C 106 (2020) 110180.
[42] M. Vallet-Regí, D. Lozano, B. González, I. Izquierdo-Barba, Biomaterials against bone infection, Adv. Healthcare Mater. 9 (2020) 2000310.
[43] M. Vallet-Regí, A.J. Salinas, Mesoporous bioactive glasses for regenerative medicine, Mater. Today Bio 11 (2021) 100121.
[44] A.J. Salinas, P. Esbrit, Mesoporous bioglasses enriched with bioactive agents for bone repair, with a special highlight of María Vallet-Regí's contribution, Pharmaceutics 14 (2022) 202.

[45] W. Xia, J. Chang, Well-ordered mesoporous bioactive glasses (MBG): a promising bioactive drug delivery system, J. Control. Rel. 110 (3) (2006) 522–530.
[46] C. Wu, J. Chang, Y. Xiao, Mesoporous bioactive glasses as drug delivery and bone tissue regeneration platforms, Ther. Deliv. 2 (9) (2011) 1189–1198.
[47] M. Vallet-Regí, I. Izquierdo-Barba, M. Colilla, Structure and functionalization of mesoporous bioceramics for bone tissue regeneration and local drug delivery, Philos. Trans. A Math. Phys. Eng. Sci. 370 (1963) (2012) 1400–1421.
[48] S. Sánchez-Salcedo, A. García, M. Vallet-Regí´, Prevention of bacterial adhesion to zwitterionic biocompatible mesoporous glasses, Acta Biomater. 57 (2017) 472–486.
[49] C. Wu, R. Miron, A. Sculean, S. Kaskel, T. Doert, R. Schulze, Y. Zhang, Proliferation, differentiation and gene expression of osteoblasts in boron-containing associated with dexamethasone deliver from mesoporous bioactive glass scaffolds, Biomaterials 32 (29) (2011) 7068–7078.
[50] Q. Nawaz, M.A.U. Rehman, A. Burkovski, J. Schmidt, A.M. Beltrán, A. Shahid, N.K. Alber, W. Peukert, A.R. Boccaccini, Synthesis and characterization of manganese containing mesoporous bioactive glass nanoparticles for biomedical applications, J. Mater. Sci. Mater. Med. 29 (5) (2018) 64.
[51] C. Heras, S. Sánchez-Salcedo, D. Lozano, J. Peña, P. Esbrit, M. Vallet-Regí´, A.J. Salinas, Osteostatin potentiates the bioactivity of mesoporous glass scaffolds containing Zn^{2+} ions in human mesenchymal stem cells, Acta Biomater. 89 (2019) 359–371.
[52] M.L. Dittler, I. Unalan, A. Grünewald, A.M. Beltrán, C.A. Grillo, R. Destch, M.C. González, A.R. Boccaccini, Bioactive glass (45S5)-based 3D scaffolds coated with magnesium and zinc-loaded hydroxyapatite nanoparticles for tissue engineering applications, Colloids Surf. B Biointerfaces 182 (2019) 110346.
[53] J. Jiménez-Holguín, A. López-Hidalgo, S. Sánchez-Salcedo, J. Peña, M. Vallet-Regí, A.J. Salinas, Strontium-modified scaffolds based on mesoporous bioactive glasses/polyvinyl alcohol composites for bone regeneration, Materials 13 (2020) 5526.
[54] C. Heras, J. Jiménez-Holguín, A.L. Doadrio, M. Vallet-Regí´, S. Sánchez-Salcedo, A.J. Salinas, Multifunctional antibiotic- and zinc-containing mesoporous bioactive glass scaffolds to fight bone infection, Acta Biomater. 114 (2020) 395–406.
[55] A.A. El-Rashidy, G. Waly, A. Gad, J.A. Roether, J. Hum, Y. Yang, R. Detsch, A.A. Hashem, I. Sami, W.H. Goldmann, A.R. Boccaccini, Antibacterial activity and biocompatibility of zein scaffolds containing silver-doped bioactive glass, Biomed. Mater. 13 (2018) 065006.
[56] T.E. Paterson, R. Shi, J. Tian, C.J. Harrison, M. De Sousa Mendes, P.V. Hatton, Z. Li, I. Ortega, Electrospun scaffolds containing silver-doped hydroxyapatite with antimicrobial properties for applications in orthopedic and dental bone surgery, J. Funct. Biomater. 11 (3) (2020) 58.
[57] A.C. Marsh, N.P. Mellott, M. Crimp, A. Wren, N. Hammer, X. Chatzistavrou, Ag–doped bioactive glass-ceramic 3D scaffolds: microstructural, antibacterial, and biological properties, J. Eur. Ceram. Soc. 46 (6) (2021) 3717–3730.
[58] G. Qian, L. Zhang, X. Liu, S. Wu, S. Peng, C. Shuai, Silver-doped bioglass modified scaffolds: a sustained antibacterial efficacy, Mater. Sci. Eng. C 129 (2021) 112425.
[59] V.M. Schatkoski, T.L.D. Montanheiro, B.R.C. de Menezes, R.M. Pereira, K.F. Rodrigues, R.G. Ribas, D.M. da Silva, G.P. Thim, Current advances concerning the most cited metal ions doped bioceramics and silicate-based bioactive glasses for bone tissue engineering, Ceram. Int. 47 (3) (2021) 2999–3012.
[60] M. Mabrouk, H.H. Beherei, Y. Tanaka, M. Tanaka, Sol-gel silicate glass doped with silver for bone regeneration: Antibacterial activity, intermediate water, and cell death mode, Biomater. Adv. 138 (2022) 212965.
[61] A. López-Noriega, D. Arcos, I. Izquierdo-Barba, Y. Sakamoto, O. Terasaki, M. Vallet-Regí, Ordered mesoporous bioactive glasses for bone tissue regeneration, Chem. Mater. 18 (2006) 3137–3144.
[62] A. García, I. Izquierdo-Barba, M. Colilla, C. López de Laorden, M. Vallet-Regí´, Preparation of 3D scaffolds in the SiO_2-P_2O_5 system with tailored hierarchical meso-macroporosity, Acta Biomater. 7 (2011) 1265–1273.
[63] M. Cicuéndez, M. Malmsten, J.C. Doadrio, M.T. Portolés, I. Izquierdo-Barba, M. Vallet-Regí´, Tailoring hierarchical meso-macroporous 3D scaffolds: from nano to macro, J. Mater. Chem. B 2 (2014) 49–58.
[64] S. Brunauer, P.H. Emmett, E. Teller, Adsorption of gases in multimolecular layers, J. Am. Chem. Soc. 60 (1) (1938) 309–319.
[65] E.P. Barrett, L.G. Joyner, P.P. Halenda, The determination of pore volume and area distributions in porous substances. I. Computations from nitrogen isotherms, J. Am. Chem. Soc. 73 (1) (1951) 373–380.
[66] W.N. Addison, V. Nelea, F. Chicatun, Y.-C. Chien, N. Tran-Khanh, M.D. Buschmann, S.N. Nazhat, M.T. Kaartinen, H. Vali, M.M. Tecklenburg, R.T. Franceschi, M.D. McKee, Extracellular matrix mineralization in murine MC3T3-E1 osteoblast cultures: an ultrastructural, compositional and comparative analysis with mouse bone, Bone 71 (2015) 244–256.
[67] M. Martínez-Pérez, C. Pérez-Jorge, D. Lozano, S. Portal-Nuñez, R. Pérez–Tanoira, A. Conde, M.A. Arenas, J.M. Hernández-López, J.J. de Damborenea, E. Gómez-Barrena, P. Esbrit, J. Esteban, Evaluation of bacterial adherence of clinical isolates of *Staphylococcus sp.* using a competitive model: An *in vitro* approach to the "race for the surface" theory, Bone Joint Res. 6 (5) (2017) 315–322.
[68] Z. Ma, S. Dai, CHAPTER 1: Stabilizing Gold Nanoparticles by Solid Supports, in Heterogeneous Gold Catalysts and Catalysis, Catalysis Series, 2014, pp. 1–26, doi:10.1039/9781782621645-00001.
[69] A. García, A. Nieto, M. Vila, M. Vallet-Regí´, Easy synthesis of ordered mesoporous carbon containing nickel nanoparticles by a low temperature hydrothermal method, Carbon (51) (2013) 410–418.
[70] L. Gharibshahi, E. Saion, E. Gharibshahi, A.H. Shaari, K.A. Matori, Structural and optical properties of Ag nanoparticles synthesized by thermal treatment method, Materials 10 (2017) 4002.
[71] A. García, M. Cicuéndez, I. Izquierdo-Barba, D. Arcos, M. Vallet-Regí´, Essential role of calcium phosphate heterogeneities in 2D-hexagonal and 3D-cubic SiO_2-CaO-P_2O_5 mesoporous bioactive glasses, Chem. Mater. 21 (2009) 5474–5484.
[72] A.S. Lanje, S.J. Sharma, R.B. Pode, Synthesis of silver nanoparticles: a safer alternative to conventional antimicrobial and antibacterial agents, J. Chem. Pharm. Res. 2 (3) (2010) 478–483.
[73] X. Yang, Y. Du, D. Li, Z. Lv, E. Wang, One-step synthesized silver micro-dendrites used as novel separation mediums and their applications in multi-DNA analysis, Chem. Commun. 47 (38) (2011) 10581–10583.
[74] U.T. Khatoon, K.V. Rao, J.V.R. Rao, Y. Aparna, Synthesis and characterization of silver nanoparticles by chemical reduction method, in: International Conference on Nanoscience, Engineering and Technology (ICONSET), 2011, pp. 97–99.
[75] S. Rajawat, M.S. Qureshi, Silver nanoparticles: novel synthesis technique and characterizations, in: P.K. Giri, D.K. Goswami, A. Perumal (Eds.), Advanced Nanomaterials and Nanotechnology. Springer Proceedings in Physics, 143, Berlin, Heidelberg, Springer, 2013, pp. 77–83.
[76] S.J. Gregg, K.S.W. Sing, Adsorption Surface Area and Porosity, 2nd ed., Academic Press, New York, 1982.
[77] M. Kruk, M. Jaroniec, A. Sayari, Relations between pore structure parameters and their implications for characterization of MCM-41 using gas adsorption and X-ray diffraction, Chem. Mater. 11 (1999) 492–500.
[78] B.D. Boyan, T.H. Hummert, D.D. Dean, Z. Schwartz, Role of material surfaces in regulating bone and cartilage cell response, Biomaterials 17 (2) (1996) 137–146.
[79] E. Madsen, M. Mededovic, D.H. Kohn, Review on material parameters to enhance bone cell function *in vitro* and *in vivo*, Biochem. Soc. Trans. 48 (5) (2020) 2039–2050.
[80] S. Shruti, A.J. Salinas, G. Lusvardi, G. Malavasi, L. Menabue, M. Vallet-Regi, Mesoporous bioactive scaffolds prepared with cerium-, gallium- and zinc-containing glasses, Acta Biomater. 9 (1) (2013) 4836–4844.
[81] M.N. Gómez-Cerezo, D. Lozano, D. Arcos, M. Vallet-Regí, C. Vaquette, The effect of biomimetic mineralization of 3D-printed mesoporous bioglass scaffolds on physical properties and *in vitro* osteogenicity, Mater. Sci. Eng. C 109 (2020) 110572.
[82] L. Casarrubios, N. Gómez-Cerezo, S. Sánchez-Salcedo, M.J. Feito, M.C. Serrano, M. Saiz-Pardo, L. Ortega, D. de Pablo, I. Díaz-Guemes, B. Fernández-Tomé, S. Enciso, F.M. Sánchez-Margallo, M.T. Portolés, D. Arcos, M. Vallet-Regí, Silicon substituted hydroxyapatite/VEGF scaffolds stimulate bone regeneration in osteoporotic sheep, Acta Biomater. 101 (2020) 544–553.
[83] B. Reidy, A. Haase, A. Luch, K.A. Dawson, I. Lynch, Mechanisms of silver nanoparticle release, transformation and toxicity: a critical review of current knowledge and recommendations for future studies and applications, Materials 6 (6) (2013) 2295–2350.
[84] Z.M. Xiu, Q.B. Zhang, H.L. Puppala, V.L. Colvin, P.J. Álvarez, Negligible particle-specific antibacterial activity of silver nanoparticles, Nano Lett. 12 (8) (2012) 4271–4275.
[85] K. Loza, J. Diendorf, C. Sengstock, L. Ruiz-González, J.M. González-Calbet, M. Vallet-Regí´, M. Köller, M. Epple, The dissolution and biological effects of silver nanoparticles in biological media, J. Mater. Chem. B 2 (12) (2014) 1634–1643.
[86] Q. Feng, T.N. Kim, J. Wu, E.S. Park, J.O. Kim, D.Y. Lim, F.Z. Cui, Antibacterial effects of Ag-HAp thin films on alumina substrates, Thin Solid Films 335 (1998) 214–219.
[87] H. Zhu, C. Hu, F. Zhang, X. Feng, J. Li, T. Liua, J. Chen, J. Zhang, Preparation and antibacterial property of silver-containing mesoporous 58S bioactive glass, Mater. Sci. Eng. C 42 (2014) 22–30.
[88] X.X. Yan, H.X. Deng, X.H. Huang, G.Q. Lu, S.Z. Qiao, D.Y. Zhao, C.Z. Yu, Mesoporous bioactive glasses. I. Synthesis and structural characterization, J. Non-Cryst. Solids 351 (2005) 3209–3217.
[89] J. Ma, C. Chen, D. Wang, Y. Jiao, J. Shi, Effect of magnesia on the degradability and bioactivity of sol-gel derived SiO_2-CaO-MgO-P_2O_5 system glasses, Colloids Surf. B Biointerfaces 81 (2010) 87–95.
[90] C. Wu, J. Chang, Mesoporous bioactive glasses: structure characteristics, drug/growth factor delivery and bone regeneration application, Interfac. Focus 2 (2012) 292–306.
[91] M. Diba, A.R. Boccaccini, Silver-containing bioactive glasses for tissue engineering applications, Precious Met. Biomed. Appl. (2014) 177–211.